

## Virtual glioblastoma: growth, migration and treatment in a three-dimensional mathematical model

S. E. Eikenberry\*, T. Sankar†‡, M. C. Preul†, E. J. Kostelich\*, C. J. Thalhauser\*§ and Y. Kuang\*

\*Department of Mathematics and Statistics, Arizona State University, Tempe, AZ 85287, USA, †Department of Neurosurgery Research, Barrow Neurological Institute, St. Joseph's Hospital and Medical Center, Phoenix, AZ 85013, USA

Received 1 April 2008; revision accepted 13 August 2008

### Abstract

**Objectives:** Glioblastomas are aggressive primary brain cancers that are characterized by extensive infiltration into the brain and are highly resistant to treatment. Through mathematical modelling, we model the process of invasion and predict the relative importance of mechanisms contributing to malignant invasion. Clinically, we predict patterns of tumour recurrence following various modes of therapeutic intervention.

**Materials and methods:** Our mathematical model uses a realistic three-dimensional brain geometry and considers migrating and proliferating cells as separate classes. Several mechanisms for infiltrative migration are considered. Methods are developed for simulating surgical resection, radiotherapy and chemotherapy.

**Results:** The model provides clinically realistic predictions of tumour growth and recurrence following therapeutic intervention. Specific results include (i) invasiveness is governed largely by the ability of glioblastoma cells to degrade and migrate through the extracellular matrix and the ability of single migrating cells to form colonies; (ii) tumours originating deeper in the brain generally grow more quickly than those of superficial origin; (iii) upon surgery, the margins and geometry of resection significantly determine the extent and pattern of postoperative recurrence; (iv) radiotherapy works synergistically with greater resection margins to

reduce recurrence; (v) simulations in both two- and three-dimensional geometries give qualitatively similar results; and (vi) in an actual clinical case comprising several surgical interventions, the model provides good qualitative agreement between the simulated and observed course of the disease.

**Conclusions:** The model provides a useful initial framework by which biological mechanisms of invasion and efficacy of potential treatment regimens may be assessed.

### Introduction

Glioblastoma multiforme (GBM) is a highly invasive brain tumour that is associated with very low median survival time (< 15 months) (1). GBM is highly diffuse and can invade a large portion of the cerebral cortex in a short period of time, making complete surgical excision impossible and recurrence inevitable (2). Previous mathematical models have tended to focus on one particular aspect of glioblastoma behaviour. Diffuse invasion in gliomas was first investigated by Tracqui *et al.* (3). In similar models by Woodward *et al.* (4) and Burgess *et al.* (5), rates of diffusion and growth were studied as key parameters describing glioma expansion. Tracqui and Mendjeli (6) consider a model of glioma invasion in a three-dimensional brain geometry with homogeneous tissue and boundaries imposed at the skull and ventricles.

Based on this earlier work, Swanson *et al.* (7) formulated a mathematical model for glioma invasion that considered a single class of highly motile cells on a realistic brain geometry given by the BrainWeb database (8–11) (available online at <http://www.bic.mni.mcgill.ca/brainweb>) in which cell motility differed between white and grey matter. This and other models of diffuse invasion are reviewed in Swanson *et al.* (12). In a reaction-diffusion model by Stein *et al.* (13), it was found that glioblastoma spheroids are characterized by two separate classes of cells: core proliferating cells and peritumoural cells migrating away

Correspondence: S. E. Eikenberry, Department of Mathematics and Statistics, Arizona State University, Tempe, AZ 85287, USA. Tel.: +1 480 567 8810; E-mail: seikenbe@asu.edu

‡Present Address: Division of Neurosurgery, University of Alberta, WMC Health Sciences Centre, Edmonton, AB, Canada, T6G 2B7

§Present Address: Department of Mathematics, University of California Irvine, Irvine, CA 92612, USA

from the spheroid in a directed manner. MacArthur *et al.* (14) considered haptotaxis as a mechanism for glioma cell migration.

This paper describes a spatially explicit model of glioblastoma invasion with stochastic partial differential equations using the BrainWeb database to initialize the brain geometry. Our model considers two distinct classes of cells: core proliferating cells and migrating cells.

A generalized chemorepellent is considered as the primary mechanism by which cells transition between the two classes. Interactions between the extracellular matrix (ECM) and glioblastoma cells are included as a mechanism for the directed migration of tumour cells. Glioblastoma cell migration is taken to be greater in white than grey matter, and the model accounts for cell diffusion into the cerebrospinal fluid. Thus, our model represents a synthesis of previous modelling efforts into a single framework.

Tumour invasion in several different regions of the brain is simulated utilising this model, using the full three-dimensional brain geometry and representative two-dimensional cross-sections. Simulations of treatment by radiotherapy, chemotherapy and surgical resection, including application of realistic resection cavities specific to individual tumours, have been performed. Spatial probability distributions of tumour recurrence following resection can be estimated. An actual clinical case involving several surgical interventions is simulated, and the model results are qualitatively similar to actual tumour progression.

The ultimate goal of this work is to develop a theoretical model that can accurately describe the mechanisms that govern malignant GBM invasion and be applied to clinical decision-making. We begin with a brief outline of the biology of glioblastomas. In the Materials and Methods, we describe the derivation of the model and its parameterization. Representative simulations and a comparison to an actual clinical case are described in the Results, and potential refinements to the model are addressed in the Discussion.

## Biological background

Our model formulation is based on the biological characteristics of malignant gliomas. This section reviews the most important aspects of GBM invasion in relation to the model.

Glioblastomas arise either from lower-grade astrocytomas or *de novo* from glial cells (15). Low-grade astrocytomas and anaplastic gliomas typically progress towards a more malignant phenotype through genetic evolution, and can acquire the characteristics of a glioblastoma. However, most glioblastomas are diagnosed as *de novo* tumours and are characterized by epidermal growth factor receptor expression and a variety of genetic defects, including loss of chromosome 10 (15). Therefore, we do not model

neoplastic evolution and instead simulate only tumours that arise *de novo*.

In both *in vivo* and *in vitro* models, migrating tumour cells detach from the primary mass early in tumour evolution (13,16,17), and invade the surrounding brain (16). There are probably several mechanisms that cause this detachment. A number of cytokines overexpressed by gliomas induce cell migration. The most important appear to be epidermal growth factor (EGF) and scatter factor/hepatocyte growth factor (SF/HGF), both of which are correlated with grade of GBM malignancy (18–20). There is also evidence of a chemorepellent produced by glioma spheroids. The strength of this chemorepellent may be greater in tumours that display regions of necrosis and hypoxia (17).

The proliferating core cells and peritumoural migrating cells are phenologically distinct. To migrate, cells must modify their shape to interact with the ECM, become polarized, and develop membrane extensions (2). Migrating cells also appear to defer their proliferation to some degree (13). Although they display little proliferation over the course of primary tumour invasion, single invasive cells have a tumourigenic capacity (16) and are widely accepted as being responsible for tumour recurrence following resection (21).

Migrating glioma cells use existing anatomical structures in the brain as substrates to facilitate migration, including white matter tracts. Myelinated white fibre tracts, particularly in the corpus callosum, are a strongly preferred substrate for glioma migration (22). White matter is less dense than grey matter and, thus, is mechanically more permissive (23). Blood vessel basement membranes are also used as a substrate (21), and in grey matter, glioma cells tend to migrate along capillary walls (24).

Migration is highly dependent on the composition of the ECM and expression of cell adhesion molecules. Many brain ECM proteins stimulate glioma cell migration (2,25) and gliomas produce ECM components permissive to migration, particularly tenascin (21). Gliomas also overexpress ECM-degrading matrix metalloproteinases (15), which appear to contribute to glioma invasiveness by clearing space and overcoming inhibitors of migration (21,22). Matrix metalloproteolytic activity is necessary for glioma migration along a myelin substrate, and this activity is correlated with grade of malignancy (22).

Malignant invasion requires neoangiogenesis, the formation of a tumour-nourishing vasculature. Tumoural vessels are characterized by high permeability and tortuous organization, which result in regions of hypoxia and necrosis. Leaky tumour vasculature combined with disruption of normal brain vessels leads to vasogenic oedema. This oedema is a significant cause of mass effect and extends primarily along white matter tracts (23) which may serve to increase glioma cell dissemination there.

Migrating glioma cells are resistant to chemotherapy and radiotherapy (22). They also show a decreased proliferation rate compared to non-migrating cells (22), which in itself confers resistance to these modes of treatment. Several factors that increase migration and resistance to apoptosis are also overexpressed by migrating glioma cells (2), and sublethal irradiation may also promote their migration and invasiveness (24).

Treatment usually involves resection of the main tumour mass followed by radiotherapy. Typically, radiation is applied either to the whole brain, the tumour volume with a 1- to 2-cm margin, or both. Radiotherapy significantly increases patient survival time (1,24) and, more recently, chemotherapy has shown a small, but definite impact on survival too. Traditional adjuvant chemotherapy, such as bis-chloronitrosourea (BCNU) or procarbazine, lomustine, vincristine (PCV) regimens, can offer a small survival benefit (1) and treatment with temozolomide has recently been shown to significantly increase survival (1).

Glioblastomas nearly always recur and are uniformly fatal. They typically recur near the resection cavity or radiotherapy volume; a small percentage recur more distantly (24).

## Materials and methods

### Mathematical model

Our mathematical formulation is a continuous reaction-diffusion model with the following assumptions.

- 1 Two distinct phenotypical classes of glioma cells are considered: migrating and proliferating. The transition between these classes is stochastic.
- 2 At sufficiently high concentrations, a generalized chemorepellent produced by proliferating glioma cells induces migration. At low concentrations, migrating cells return to the proliferating class at a small, random rate. (This chemorepellent can be considered an aggregation of secreted chemorepellents and other factors that induce migration, such as EGF and SF/HGF.)
- 3 Cells invade and migrate into white matter more quickly than into grey matter.
- 4 Interactions between glioma cells and the ECM permit long-range migration. Migrating cells degrade the ECM and travel up the ECM gradient by haptotaxis and this migration is faster in white than in grey matter.

A deterministic version of the first assumption was implemented by Thalhauser *et al.* (25), who studied the balance of proliferating and migrating phenotypes in an *in vivo* tumor cord model. In later subsections, we extend the model to a discretized system that includes stochastic transitions between the migrating and proliferating cell classes.

There are four model variables that depend on the spatial location,  $\mathbf{x}$ , in either two or three dimensions, and on time,  $t$ :

$g(\mathbf{x}, t)$  = proliferating tumour cell density

$m(\mathbf{x}, t)$  = migrating tumour cell density

$c(\mathbf{x}, t)$  = chemorepellent density

$w(\mathbf{x}, t)$  = ECM density

The continuous model is formulated as follows.

$$\frac{\partial g}{\partial t} = \underbrace{D_G(\mathbf{x})\nabla^2 g}_{\text{diffusion}} + \underbrace{\alpha g \left(1 - \frac{T}{T_{\max}}\right)}_{\text{logistic-growth}} - \underbrace{\Phi(g, m, c)}_{\text{loss-to-migrating}} + \underbrace{\Psi(g, m, c)}_{\text{gain-from-migrating}} \tag{1}$$

$$\frac{\partial m}{\partial t} = \underbrace{D_M(\mathbf{x})\nabla^2 m}_{\text{diffusion}} + \underbrace{\chi(\mathbf{x})\nabla \cdot (m\nabla w)}_{\text{haptotaxis}} + \underbrace{\Phi(g, m, c)}_{\text{gain-from-growing}} + \underbrace{\Psi(g, m, c)}_{\text{loss-to-growing}} - \underbrace{\sigma m \left(\frac{T^2}{T_{\max}^2}\right) H(M_D - T_{\max})}_{\text{crowding-death}} \tag{2}$$

$$\frac{\partial c}{\partial t} = \underbrace{D_C\nabla^2 c}_{\text{diffusion}} + \underbrace{\gamma g}_{\text{production}} - \underbrace{\beta_C c}_{\text{degradation}} \tag{3}$$

$$\frac{\partial w}{\partial t} = \underbrace{-\rho w \left(\frac{T}{\theta_w + T}\right)}_{\text{degradation}} + \underbrace{\alpha_w w(1-w)}_{\text{repair}} \tag{4}$$

where

$$T = g + m \tag{5}$$

$$\Phi(g, m, c) = \tau g \left(\frac{\theta_G^2}{T^2 + \theta_G^2}\right) \left(\frac{c}{\phi_M + c}\right) \tag{6}$$

Each equation models the principal biological behaviour discussed in the previous section.

*Proliferation.* Equation (1) describes the behaviour of proliferating cells. The diffusion term represents cell movement due to random migration. The migration of proliferating cells is assumed to be due to crowding and simple mechanical pressure; there is little active migration, and diffusive flux is low. The diffusion coefficient  $D_G(\mathbf{x})$  depends on position and is larger in white matter. Growth is logistic with the maximum per capita growth rate  $\alpha$ . Loss of cells switching to the migratory phenotype is given by  $\Phi$ , and  $\Psi$  is the gain from cells switching from the migrating class.

The rate at which proliferating cells become migratory depends continuously on both total cell density and chemorepellent concentration. The hill function,  $\theta_G^2(T^2 + \theta_G^2)$ , causes the transition to the migratory phenotype to be greatest when total cell density is low and has the effect of inducing migration primarily at the tumour core edge. The term  $c/(\phi_M + c)$  causes transition to the proliferating phenotype to occur primarily when chemorepellent concentration is high.

We do not consider any particular form for  $\Psi(g, m, c)$  within the continuous model framework, as we assume that each migrating cell has a specific probability of becoming proliferating. This requires knowing the absolute number of cells at a discrete gridpoint, and there is no continuous analogue to this formulation.

*Migration.* Equation (2) governs the behaviour of migrating cells. As with proliferating cells, there is undirected migration (diffusion) that is greater in white matter. As chemokinesis appears to be an important component of glioma migration (26), we assume that  $D_M(\mathbf{x}) > D_G(\mathbf{x})$ . The haptotaxis term provides for directed migration at the invasive front. We do not include chemotaxis down the chemorepellent gradient; we have found that such a term causes little change in the dynamics and merely introduces a parameter that is difficult to estimate. The final term reflects death of migrating cells when total cell density approaches carrying capacity. The inclusion of this term prevents regions of unrealistically high cell density from forming.

*Chemorepellent.* Equation (3) implies that the chemorepellent diffuses at a constant rate throughout the domain. Proliferating cells produce the factor at the constant rate  $\gamma$ , and it degrades at the constant rate  $\beta_C$ .

*Extracellular matrix.* Our model of the ECM, eqn (4), is an abstraction that is meant to allow the biologically realistic phenomenon of directed migration into an unpermissive matrix, which is modified by metalloproteolytic activity. ECM density,  $w$ , is normalized to unity. A density of 1 represents the normal brain ECM, while a density of 0 represents maximally degraded ECM. Invading glioma cells do not completely degrade the ECM, as excessive degradation can inhibit rather than aid migration (21). Therefore, haptotaxis up an ECM gradient represents directed migration into normal brain ECM that is being actively modified.

We assume the ECM is degraded at the maximum rate  $\rho$ . The hill term,  $T/(\theta_W + T)$ , causes degradation to occur at (nearly) the maximal rate when glioma cell density is sufficiently large. We also assume that the ECM repairs itself (i.e. normalizes) at the maximum rate  $\alpha_W$ .

All terms that provide for cell motility depend on the spatial location. We always take migration, both directed

and undirected, to be greater in white matter than grey matter. In the cerebrospinal fluid, there is no directed motility, but we allow very low diffusion into the cerebrospinal fluid due to the expectation that bulk pressure causes some tumoural expansion into the ventricles and resection cavities (which are filled with cerebrospinal fluid).

### Stochastic model extension

Now we consider the discretized version of the partial differential equation (PDE) and apply a stochastic effect to the rate of transition from the migrating class of cells to the growing class of cells. To solve the system, we discretize the domain and computationally apply an explicit finite difference method. Second-order differencing in space is used with first-order differencing in time. The code for this solver is written in the C programming language and uses the Message-Passing Interface (MPI) for parallel execution. The domain is divided into a regular  $n \times m \times p$  grid with respective spacing  $h_x, h_y, h_z$  in each dimension. We label the gridpoints as  $(x_i, y_j, z_k)$ , where  $0 \leq i < n$ ,  $0 \leq j < m$ , and  $0 \leq k < p$ . At each gridpoint, density,  $m$ , of migrating cells is known, and total number of cells,  $M$ , at each gridpoint can be determined by integrating over the gridpoint volume:

$$M(x_i, y_j, z_k) = \lfloor \int_V M(x_i, y_j, z_k) dV \rfloor$$

Here,  $\lfloor x \rfloor$  is the floor function, which gives the nearest integer below  $x$ . Its inclusion ensures that total number of cells is always an integer and implies that at least one whole cell must be present in a gridpoint for it to be taken into account. As the minimum gridpoint volume in simulations is  $1 \text{ mm}^3$ , this is not an unrealistic lower bound. We assume that probability of transition to the proliferating class is an exponential random variable with rate parameter  $\lambda$ . The rate parameter is not constant and depends on chemorepellent concentration:

$$\lambda = \lambda_0 \left( \frac{\phi_G}{\phi_G + c} \right)$$

This formulation is easy to implement in simulations. At every time step, the number of migrating cells and the rate parameter at every gridpoint are determined, and the probability of transition is calculated. Transition for each cell occurs randomly and independently. We refer to a migrating cell becoming proliferating as a *colony-forming event*.

### Parameterization

Some model parameters can be estimated from empirical biological data. Sensitivity of the model to others is examined

in the sensitivity analysis. Our comparison with a clinical case demonstrates that parameter values within the ranges given here yield realistic results. The average diameter of astrocytes is reported as 15–20  $\mu\text{m}$  (27). The Einstein–Stokes relation is used to calculate a diffusion coefficient,  $D$ , for an astrocyte as  $0.00238 \leq D \leq 0.00378 \text{ mm}^2/\text{day}$ . We take  $D$  to be somewhat lower *in vivo* due to pressure from surrounding normal cells. Brain ECM is more permissive in white matter than grey matter, so always we set  $D$  in white matter greater than in grey matter. In the model by Swanson *et al.* (7), diffusion coefficient of glioma cells was five times larger in white matter.

The migration of cells is highly dependent on composition of the ECM and cell expression of adhesion molecules. Swanson *et al.* (7) used  $D_M = 0.65 \text{ mm}^2/\text{day}$  in white matter. However, Stein *et al.* (13) considered this value to be too large by a factor of 10. We have assumed  $0.1 \leq D_M \leq 0.3 \text{ mm}^2/\text{day}$  but our results are not sensitive to the precise value of this parameter.

A glioblastoma line is characterized in Machado *et al.* (28). The doubling time is 24 h and the carrying capacity is  $1.0 \times 10^6 \text{ cells}/\text{mm}^3$ . Normal glial cell density was measured in Cotter *et al.* (29) as  $(8.5 \pm 1.0) \times 10^5 \text{ cells}/\text{mm}^3$ . Therefore, we take  $T_{\text{max}}$  to be  $10^6 \text{ cells}/\text{mm}^3$  in three-dimensional simulations and  $10^4 \text{ cells}/\text{mm}^3$  in two

dimensions. In the model by Stein *et al.* (13), maximum growth rate for glioma cells was 0.3 per day. Therefore, we generally choose  $0.1 \leq \alpha \leq 0.3$ .

To choose parameter values related to the chemorepellent, we assume that a density of  $1.0/\text{mm}^3$  ( $\text{mm}^2$  in two dimensions) is achieved by an isolated group of tumour cells at the carrying capacity. Since diffusion can be neglected in this case, we have  $\gamma = \beta/T_{\text{max}}$ . We assume  $\beta = 0.25$  and that  $D_C = 2.0 \text{ mm}^2/\text{day}$ .

The haptotaxis coefficient is chosen so that haptotaxis is the dominant mechanism for diffuse invasion. Table 1 gives the parameters that vary spatially for all brain matter types. The remaining parameters are given in Table 2; values that differ between two-dimensional and three-dimensional simulations are indicated in boldface.

### Model geometry

We have used the BrainWeb database (8–11). It describes distribution of white and grey matter, cerebrospinal fluid, and other structures in the brain at a resolution of  $1 \text{ mm}^3$ . However, the database does not properly resolve the falx cerebri separating the two cerebral hemispheres. We have edited the database to represent this feature by dividing the hemispheres by a wall of impermissible dura mater. In

**Table 1.** All location-dependent parameters and values. Values do not vary between two- and three-dimension

Parameter	Meaning	White matter	Corpus callosum	Grey matter	Cerebrospinal fluid
$D_G(\mathbf{x})$	Growing diffusion coefficient ( $\text{mm}^2/\text{day}$ )	0.002	0.002	0.0004	0.0001
$D_M(\mathbf{x})$	Migrating diffusion coefficient ( $\text{mm}^2/\text{day}$ )	0.1	0.1	0.02	0.0001
$\chi(\mathbf{x})$	Haptotaxis coefficient ( $\text{mm}^4/\text{day}/\text{mm}^5/\text{day}$ )	10.0	10.0	2.0	0.0

**Table 2.** All location-independent parameters and values. Parameters that differ between two- and three-dimension are shown in bold

Parameter	Meaning	Two-dimensional value	Three-dimensional value
$\alpha$	Maximum glioma growth rate	0.2/day	0.2/day
$\alpha_W$	Maximum extracellular matrix recovery rate	0.01/day	0.01/day
$\beta_C$	Chemorepellent degradation rate	0.25/day	0.25/day
$D_C$	Chemorepellent diffusion coefficient	2.0 $\text{mm}^2/\text{day}$	2.0 $\text{mm}^2/\text{day}$
$\gamma$	<b>Chemorepellent production rate</b>	$2.5 \times 10^{-5}/\text{day}/\text{cell}$	$2.5 \times 10^{-7}/\text{day}/\text{cell}$
$\lambda_0$	<b>Maximum migrating to grow rate parameter</b>	$2.5 \times 10^{-6}/\text{day}$	$2.5 \times 10^{-8}/\text{day}$
$M_D$	<b>Threshold for crowding death</b>	$0.5 \times 10^4 \text{ cells}/\text{mm}^2$	$0.5 \times 10^6 \text{ cells}/\text{mm}^3$
$\phi_G$	<b>Chemorepellent for half-maximum migrating <math>\rightarrow</math> grow</b>	0.1/ $\text{mm}^2$	0.1/ $\text{mm}$
$\phi_M$	<b>Chemorepellent for half-maximum grow <math>\rightarrow</math> migrating</b>	0.5/ $\text{mm}^2$	0.5/ $\text{mm}$
$\rho$	Max extracellular matrix remodelling rate	0.02/day <sup>1</sup>	0.02/day
$\sigma$	Max crowding death rate	1.0/day <sup>1</sup>	1.0/day
$T_{\text{max}}$	<b>Glioma carrying capacity</b>	$1.0 \times 10^4 \text{ cells}/\text{mm}^2$	$1.0 \times 10^6 \text{ cells}/\text{mm}^3$
$l$	Max transition rate, grow $\rightarrow$ migrating	0.1/day <sup>1</sup>	0.1/day
$\theta_G$	Cell density for half-maximum grow $\rightarrow$ migrating	$1.0 \times 10^2 \text{ cells}/\text{mm}^2$	$1.0 \times 10^3 \text{ cells}/\text{mm}^3$
$\theta_W$	Cell density for half-maximum extracellular matrix degradation	$1.0 \times 10^2 \text{ cells}/\text{mm}^2$	$1.0 \times 10^3 \text{ cells}/\text{mm}^3$

this way, the model permits tumour cells to migrate only along the corpus callosum.

We have also edited the database to represent the corpus callosum as a separate anatomical structure, because it is a strongly preferred route for directed white matter migration. In this version, the diffusion rates across corpus callosum are the same as in other white matter, but we can consider larger migration rates in this structure.

Areas without white or grey matter or cerebrospinal fluid are treated as completely impermissible to glioma migration. A no-flux condition is imposed at the boundary of such regions.

### Modelling treatment

To simulate treatment, a small tumour is allowed to grow for a specified amount of time, typically 6 months. At this point, a surgical resection is performed and the resection cavity is filled with cerebrospinal fluid. Two approaches to resection are considered. One is to assume that the resection cavity is the entire volume in which the glioma cells exceed a prescribed threshold density. The other is to prescribe a resection cavity whose boundaries are more representative of actual surgical practice.

A course of radiotherapy can be applied following resection. A typical clinical regimen is 6 weeks in a cycle of 5 days on, 2 days off (1). To simulate application of radiation, the growth term for proliferating cancer cells is modified to include the death of rapidly dividing cells. A small death rate is also added to the equation for migrating cells. The modified equations are:

$$\begin{aligned} \frac{\partial g}{\partial t} = & D_G(\mathbf{x})\nabla^2 g \\ & + g \underbrace{\left(1 - \frac{T}{T_{\max}}\right)}_{\text{growth/death}} (\alpha p_R(\mathbf{x}) - (1 - p_R(\mathbf{x})\alpha)) \\ & - \Phi(g, m, c) + \Psi(g, m, c) \end{aligned} \quad (7)$$

$$\begin{aligned} \frac{\partial m}{\partial t} = & D_M(\mathbf{x})\nabla^2 m - \chi(\mathbf{x})\nabla \cdot (m\nabla w) + \Phi(g, m, c) \\ & - \Psi(g, m, c) - \sigma m \left(\frac{T^2}{T_{\max}^2}\right) H(M_D - T_{\max}) \\ & - \underbrace{\omega(\mathbf{x})m}_{\text{radiation-induced-death}} \end{aligned} \quad (8)$$

Our central assumption is that radiation induces death in proliferating cells only when they pass through the cell cycle. The *per capita* growth rate is  $\alpha(1 - T/T_{\max})$  and, thus, is the rate at which proliferating cells pass through the cell cycle. We assume that in the presence of radiation,

cells either successfully divide (creating two daughter cells) or fail to divide (and die).

The probability that a cell successfully divides in the presence of radiation is  $P_R$ . If  $P_R = 0.5$ , then half of the proliferating cells die and half survive, so the net growth rate is 0. If  $P_R < 0.5$ , then radiation is sufficiently toxic to proliferating cells that the population shrinks. To simulate whole-brain and partial-brain radiation,  $P_R$  varies in space and is smaller in regions of higher dose. The additional death term for migrating cells varies similarly. In simulations, we always take the field of partial-brain radiation to be the resection cavity plus a 2-cm margin.

Chemotherapy is simulated using the same method, but given the relatively low efficacy of standard chemotherapy (1), we generally assume  $P_R$  is close to 1, so that cell growth is only slowed, not stopped.

## Results

### Sensitivity analysis

To determine the importance of the different mechanisms driving invasion in this model, we have varied the parameters governing haptotactic migration and colony formation (i.e. transition from the migrating to the proliferating class). Chemorepellent concentration at which the probability of colony formation is half-maximal,  $\phi_G$ , is varied from  $10^{-7}$  to  $10^{-1}$ . Very small values of  $\phi_G$  result in significantly smaller tumours; chemorepellents produced by the primary tumour have a significant effect on colony formation up to several centimetres away.

The transition rate parameter,  $\lambda_0$ , is varied from  $10^{-7}$  to  $10^{-2}$ . Varying  $\lambda_0$  had a somewhat greater effect on final tumour mass. Results at 6 months and 1 year in a representative location are shown in Fig. 1. Tumours for representative values of  $\lambda_0$  are shown in Fig. 2. Interestingly, tumour growth in this model is not greatly affected by the rate of chemorepellent production  $\gamma$ .

The value of  $\rho$ , which determines the ability of glioma cells to modify the ECM through matrix metalloproteinase activity, is very important in determining the level of infiltration and tumour mass. Varying  $\chi$ , which determines ability of glioma cells to migrate through a modified ECM, has a similarly important effect. Results are shown in Fig. 3.

The value of  $D_M$  is not very important, as haptotaxis is the dominant mechanism of migration, and its primary effect is to smooth the numerical solution. Maximum *per capita* growth rate,  $\alpha$ , is of course very important in determining the rate of bulk tumour expansion. We have chosen a relatively high value for  $\alpha$ , as we assume the tumour is a high-grade glioblastoma. These results suggest that the most important factors determining invasiveness

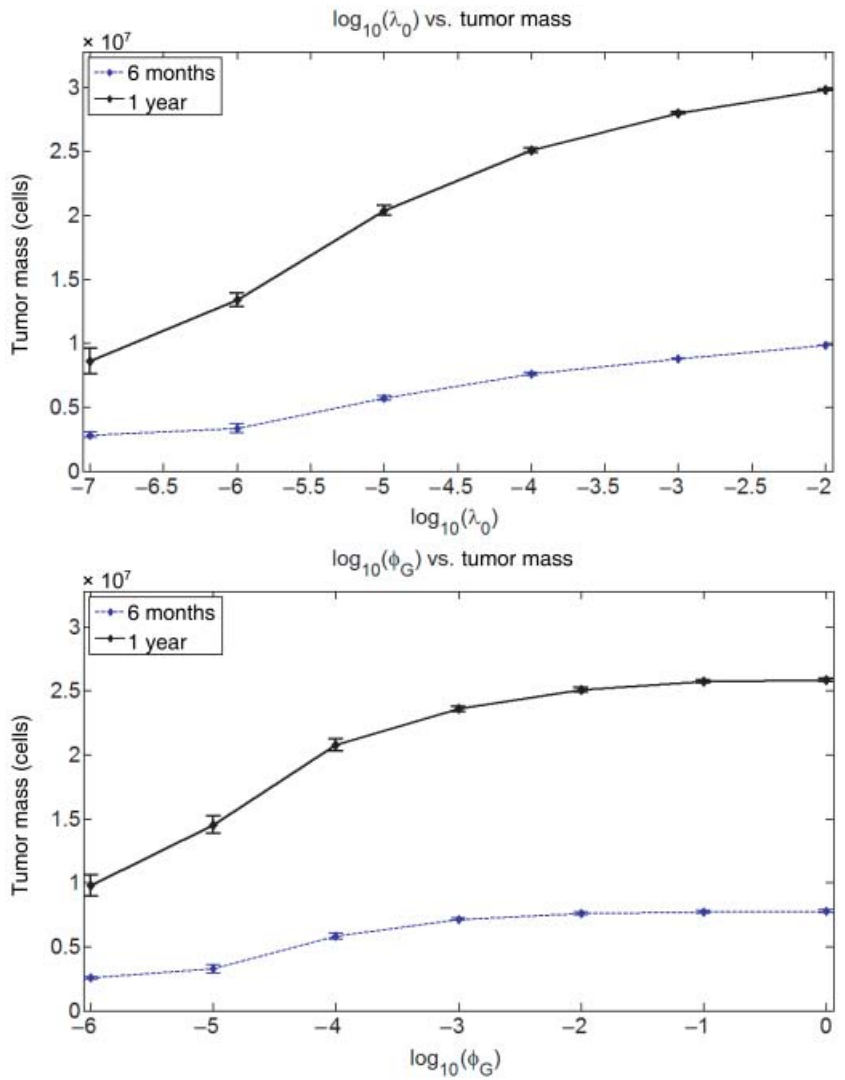


**Figure 1.** Effect of varying  $\lambda_0$  and  $\phi_G$  on tumour mass. Ten simulations of a tumour originating in location 1 are performed and the results averaged. Average tumour mass after 6 months and 1 year of invasion is displayed. (a)  $\lambda_0$ , (b)  $\phi_G$ .

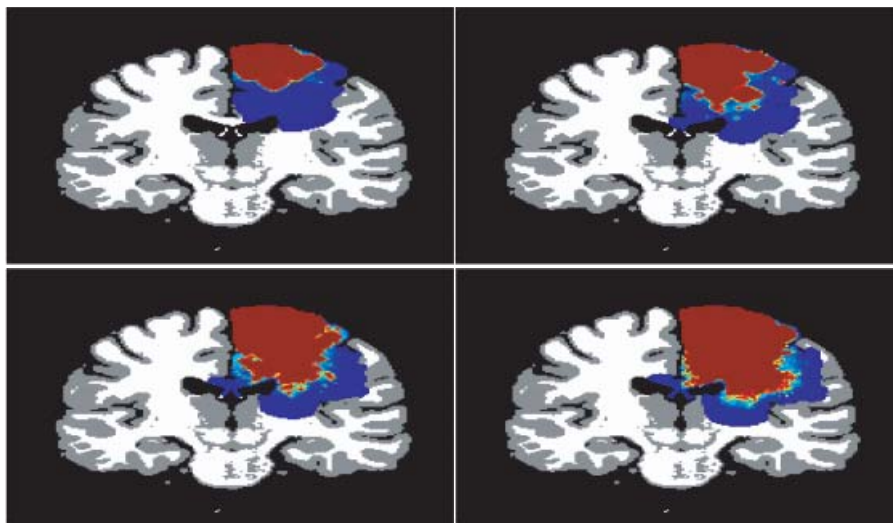


**Figure 2.** Tumour originating in location 1 after 1 year of invasion for different values of  $\lambda_0$ . (a)  $\lambda_0 = 10^{-7}$ , (b)  $\lambda_0 = 10^{-6}$ , (c)  $\lambda_0 = 10^{-5}$ , (d)  $\lambda_0 = 10^{-4}$ .

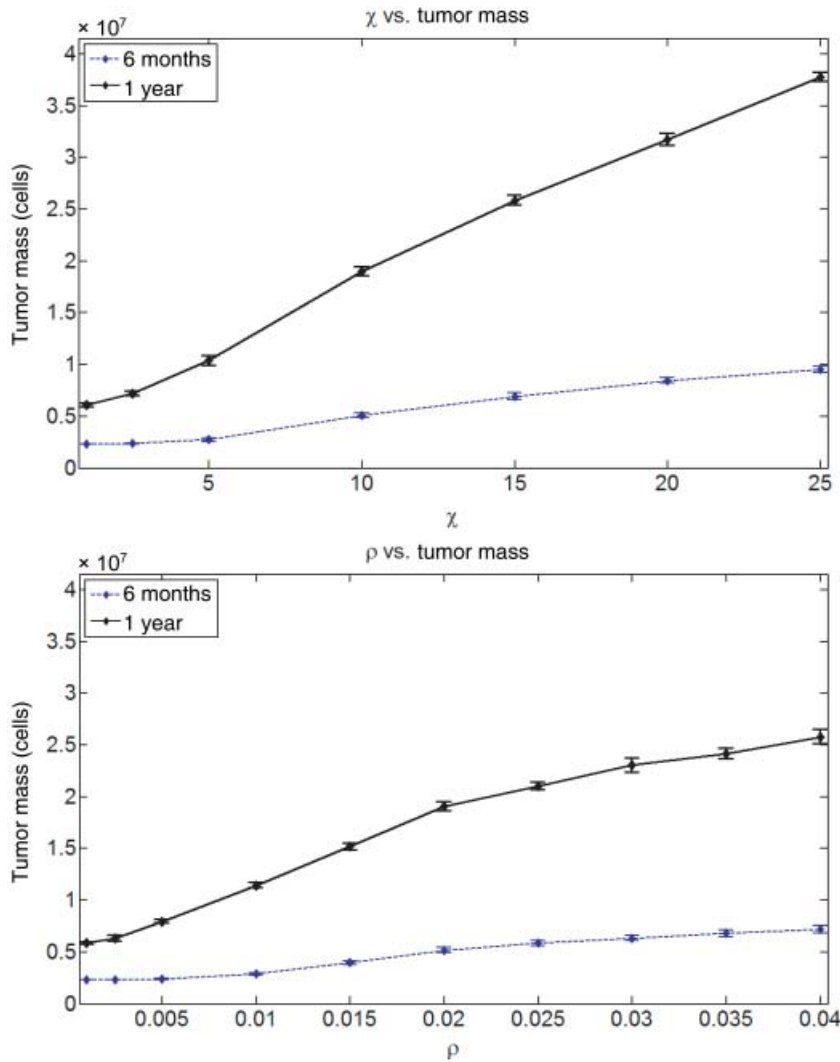


**Figure 3.** Effect of varying  $\chi$  and  $\rho$  on tumour mass. Ten simulations of a tumour originating in location 1 are performed and the results averaged. Average tumour mass after 6 months and 1 year of invasion is displayed. (a)  $\chi$ , (b)  $\rho$ .

of a GBM, other than the cell growth rate, are its ability to modify and migrate through the ECM, and the intrinsic tendency of migrating cells to form colonies.

Expression of the chemorepellent influences tumour growth much more weakly than we initially expected. The growth-inhibitory effect of a small value of  $\phi_G$  implies that any chemorepellent whose sole effect is to encourage migration over growth reduces GBM malignancy. Insofar as migration-upregulating factors are positively correlated with the grade of malignancy, we conclude that their role in promoting malignancy is not as a chemorepellent. Rather, these factors likely aid migration through the brain. Larger values of the parameters that govern haptotactic migration ( $\chi$ ,  $\rho$ ) greatly increase tumour growth and invasiveness, supporting this notion.

*Growth in different regions*

Two-dimensional simulations of tumour growth for 180 days have been performed for tumours originating in 14 different locations in a centrally located coronal cross-section of the brain. Ten separate simulations have been run for each region, and the results are averaged in space to give an invasion probability distribution. Tumour locations are shown in Fig. 4. An initial radius of 2 mm is assumed (the radius is inflated in the figure for clarity).

Two metrics are used to evaluate invasiveness: total tumour mass (number of cells) and fraction of the brain domain infiltrated by tumour cells. (A gridpoint is considered infiltrated if at least one cancer cell is present.) Final tumours for each location are shown in Figs 5 and 6.

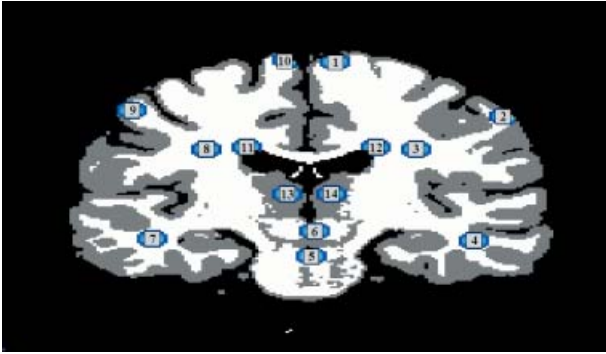


**Figure 4.** The 14 tumour initial conditions. Note that the initial tumour size is inflated for clarity.

Minimum tumour density for display is  $5/\text{mm}^2$ , which is significantly below the detection threshold by magnetic resonance imaging (MRI) (7). Tumours originating deeper in the brain generally spread more widely and have a

greater final mass than those of superficial origin. In particular, tumours originating in the cerebral hemispheres and adjacent to ventricles are very massive. Tumours in the brain stem and temporal lobes are smaller than these deep tumours but larger than superficial tumours. Tumours originating in the thalamus have low mass but spread more widely than superficial tumours of comparable mass. The final tumour mass and brain fraction infiltrated for all tumours grouped by region are given in Fig. 7.

### Three-dimensional simulations

To validate the results of two-dimensional simulations, we have performed several simulations on the full three-dimensional domain. We examine the three-dimensional tumour on the same coronal cross-section used in two-dimensional simulations. Tumour morphology on this cross-section is similar between two- and three-dimensional

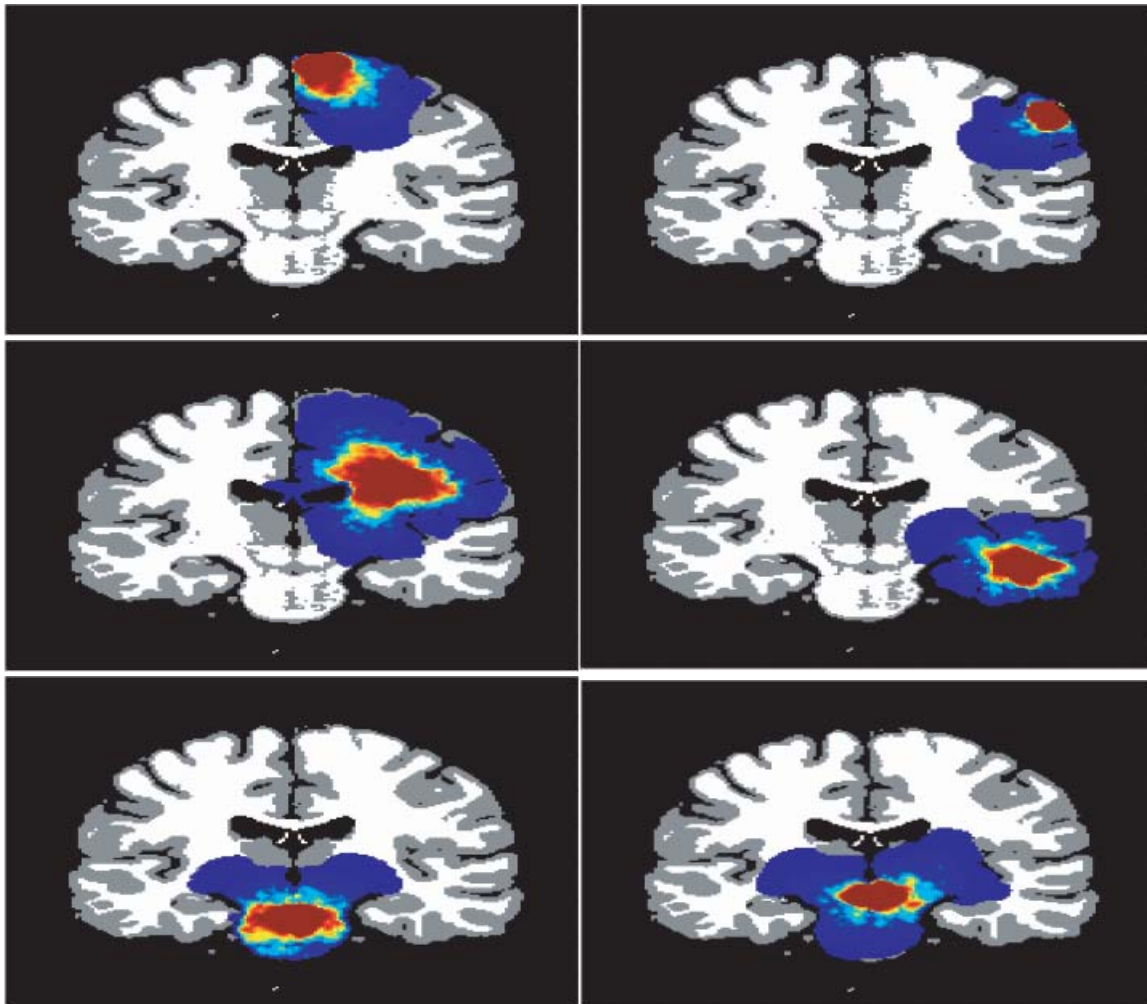


**Figure 5.** Tumours originating in locations 1–6. Ten simulations are run for 180 days and the results averaged in space. The threshold for detection is  $5/\text{mm}^2$ . (a) Location 1, (b) location 2, (c) location 3, (d) location 4, (e) location 5, and (f) location 6.

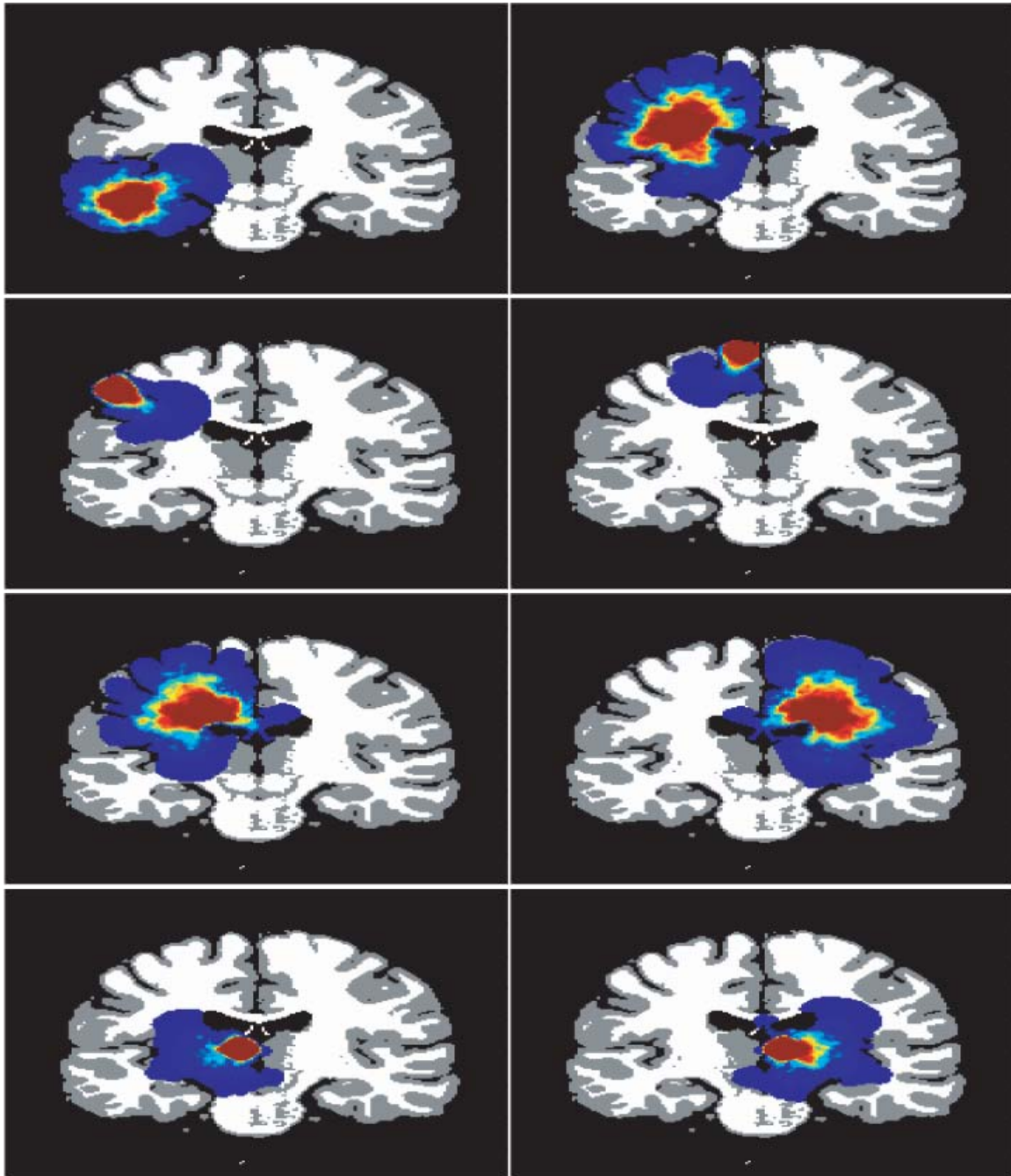


**Figure 6.** Tumours originating in locations 7–14. Ten simulations are run for 180 days and the results averaged in space. The threshold for detection is  $5/\text{mm}^2$ . (a) Location 7, (b) location 8, (c) location 9, (d) location 10, (e) location 11, (f) location 12, (g) location 13, and (h) location 14.

simulations with analogous initial conditions. The primary difference observed is that, in three-dimensional simulations, tumours spread to cover less area, probably due to the greater heterogeneity of the three-dimensional geometry (broad swaths of white matter in two-dimensions are interrupted in three-dimensions). We conclude that two-dimensional

simulations give an accurate approximation of the actual three-dimensional dynamics in a given cross-section. The results of a representative three-dimensional simulation of a tumour originating in the cerebral hemisphere are given in Fig. 8. Typical coronal, axial and sagittal cross-sections and a three-dimensional isosurface are displayed.

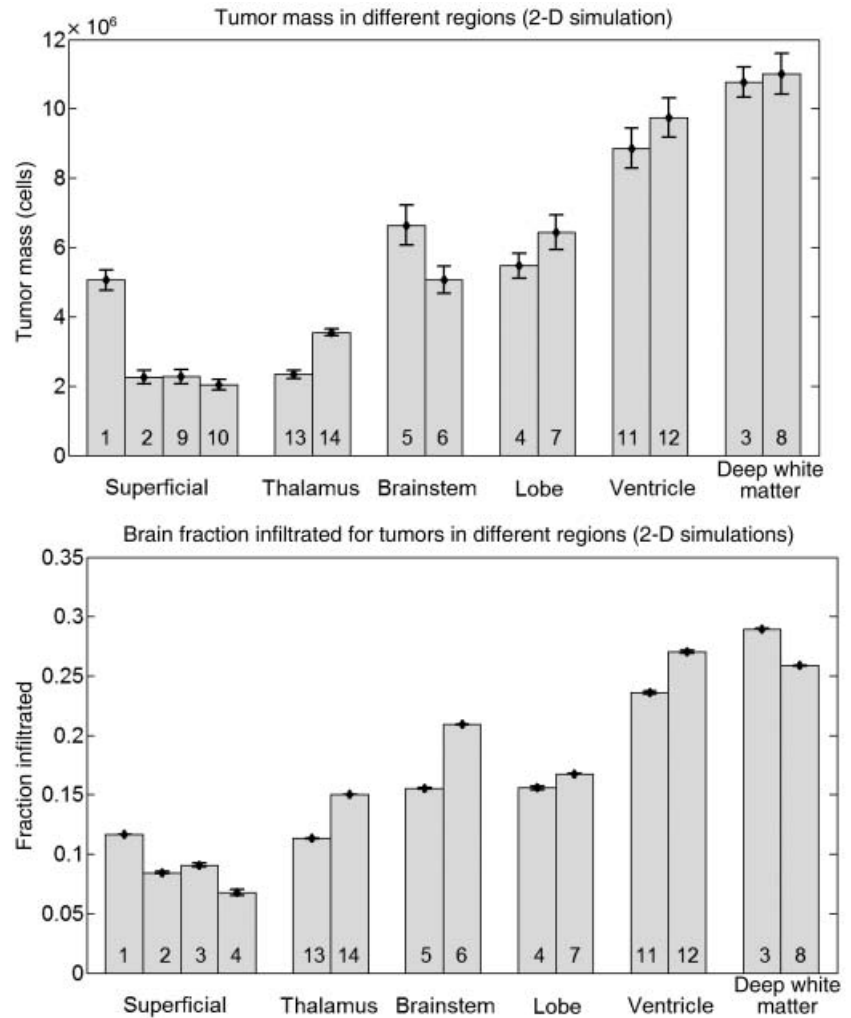


**Figure 7.** Mean tumour mass after 6 months of invasion in 14 different locations in the brain. Ten simulations are run for each tumour initial condition, and the bars give the standard deviation. The tumours are grouped by region and tumour is labelled by location. (a) Tumour mass after 6 months and (b) fraction infiltrated after 6 months.

### Treatment

The standard course of treatment is assumed to consist of surgical resection of the primary mass followed by fractionated partial brain radiotherapy. To determine the importance of resection margins on extent of recurrence, we have performed a set of numerical experiments in which surgical treatment is applied to a representative tumour. Surgery is performed at 6 months by applying the density-threshold algorithm, and the threshold cell density ranges from 5000 cells/mm<sup>2</sup> to 10 cells/mm<sup>2</sup>.

Total tumour mass following resection is tracked. Size of the resection cavity for each treatment is also measured, and number of days that elapse until the recurring tumour achieves its original mass is determined. A comparable tumour is allowed to grow without intervention for 2 years, and the tumour mass for each treatment is compared to the untreated mass at each time interval.

This experiment is performed with and without a course of partial-brain radiotherapy following resection. The experiment also is performed with radiotherapy alone (no resection). The radiation field is the resection cavity with a 2-cm margin in all directions. We set  $P_R = 0.2$  and  $\omega = 0.1$  in the field of radiation. (The random number seed was also fixed so that results could be reliably compared.)

Results are shown in Fig. 9 and indicate that increased margins have a nonlinear effect on recurrence. Significant benefit is seen only with fairly extensive resection; smaller resections offer little benefit. This finding agrees with that of Lacroix *et al.* (30), who found a significant improvement in survival for GBM patients with 98% or more of the tumour removed.

We also observe a clear benefit to treatment with radiotherapy. Radiotherapy alone reduces tumour mass, and no difference is seen when varying the size of the

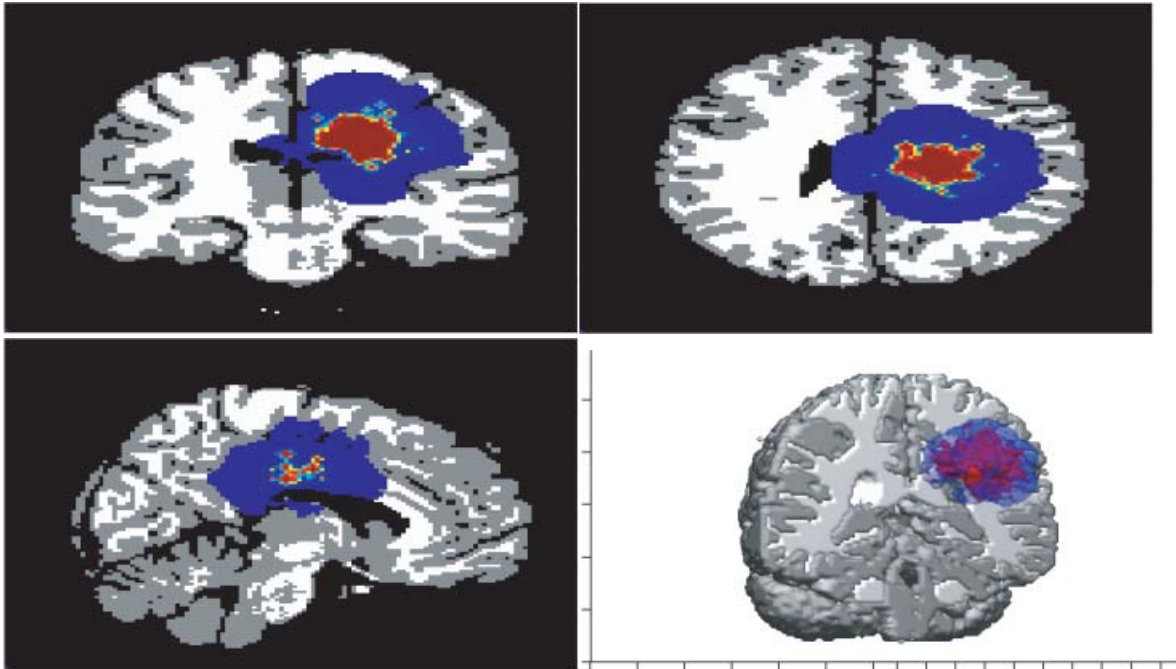


**Figure 8.** Three-dimensional, 180-day simulation of a tumour originating adjacent to the ventricle. Representative coronal (a), axial (b), and sagittal (c) cross-sections are shown. In the isosurface (d), blue represents migrating cells, and red represents proliferating cells. The blue region represents the area of the brain that has been infiltrated by migrating cells, while the red region is the proliferating tumour core. A brain backdrop is included for spatial reference.

radiation field. We also examine recurrence in response to more realistic resection cavities. In one set of experiments, several different resection cavities are applied to a tumour originating in the temporal lobe. The resection is applied at 6 months, and results are compared to the untreated tumour at 1 year.

Following resection, 10 realizations of recurrence are simulated and the results are averaged, giving an approximate spatial probability distribution of tumour recurrence. Three resection cavities are used: the first removes the visible tumour with little additional margin; the second is the visible tumour with an increased margin; and the third is a more radical resection removing all of the temporal lobe and extending into the cerebral hemisphere. We find that resecting only the visible tumour (about 400 cells/mm<sup>2</sup>) results in minimal benefit and is little better than no treatment at 1 year (7). The tumour mass versus time for the three resection cavities with and without radiotherapy is shown in Fig. 10. Average tumour recurrences at 1 year for each resection with and without radiotherapy are shown in Fig. 11 at a resolution of 5 cells/mm<sup>2</sup>.

In all cases, recurrence is primarily adjacent to and within the resection cavity. With increasing margins of resection, re-expansion of the tumour into the cavity occurs

to a lesser degree and radiotherapy has a relatively greater benefit. Examining recurrent tumours at a very low threshold for detection reveals that, with even the most radical resection, the brain is infiltrated to roughly the same degree after resection when treating with surgery alone (no adjuvant radiotherapy). Radiotherapy has an additional benefit in reducing the degree of infiltration. Figure 12 provides total tumour mass 6 months after resection, compared to no treatment and to treatment with and without radiotherapy.

#### *Simulated clinical history*

We have examined a clinical case and compared the actual course of the disease to that predicted by our model. The case involved a glioblastoma originating in the low frontal-parietal cortical region. Following diagnosis, the patient was treated surgically with most of the visible tumour removed. Standard temozolomide chemotherapy was initiated following resection, and 2 weeks later a gamma-knife treatment was applied. Recurrent tumours were treated surgically at 8 and 14 months. The history ended at 20 months, at which point most of the cerebral hemisphere had been invaded. MRI data over the entire history were available.

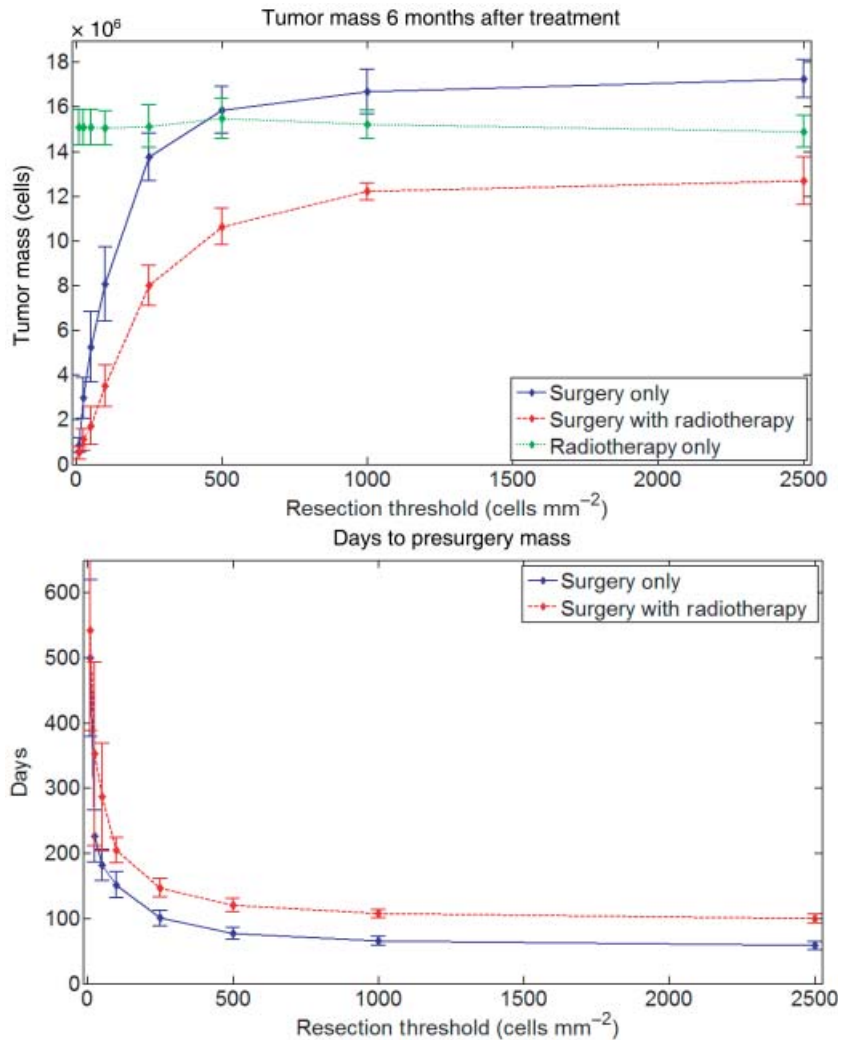


**Figure 9.** Measures of recurrence following resection using the cell-density threshold algorithm. Results are displayed for 10 simulations of a tumour in location 1 with resection performed at 180 days. (a) Days to presurgery mass following resection, and (b) fraction of the untreated tumour mass 6 months after resection.

We use the techniques previously described to simulate this course of GBM invasion. Coronal cross-sections are available for all MRIs, and tumour progression on a centrally located slice is examined. An analogous cross-section of the BrainWeb database is used for simulations, and resection cavities are determined manually. The actual brain was deformed by tumour invasion, as were resection cavities, while the model brain geometry is static. Thus, we cannot replicate collapse of the cavity seen towards the end of the clinical history.

We initialize a tumour 2 mm in radius at the estimated tumour origin. The parameter values are unchanged from the baseline values reported in Tables 1 and 2, with exceptions of  $\chi$  and  $\lambda_0$ . We slightly reduce  $\chi$  to 7.5 and increase  $\lambda_0$  to  $1.0 \times 10^{-5}$ , as these changes give results more in line with the clinical history. We expect that all individual cancers will be characterized by somewhat different parameter values.

After 180 days of invasion, the first resection is performed. At 194 days, a gamma-knife treatment is applied. We approximate the gamma knife by 3 days of high-intensity radiation applied to the resection cavity with a 2-cm margin, and set  $P_R = 0.01$  and  $\omega = 0.5$ . At 413 days, the second resection is applied to the recurring tumour, and at 595 days, the final resection is applied. The simulation is run to completion at 784 days.

We also apply continuous chemotherapy following the first resection with parameters  $P_R = 0.7$  and  $\omega = 0.05$ . This simulation is repeated 10 times using the same resection cavities, and the results are averaged in space. The actual and simulated tumours at diagnosis, second and third recurrences, and at the final time are shown in Fig. 13.

The simulated tumour is qualitatively similar in form and extent to the actual one. Furthermore, simulated invasion occurs over the same time period. The main

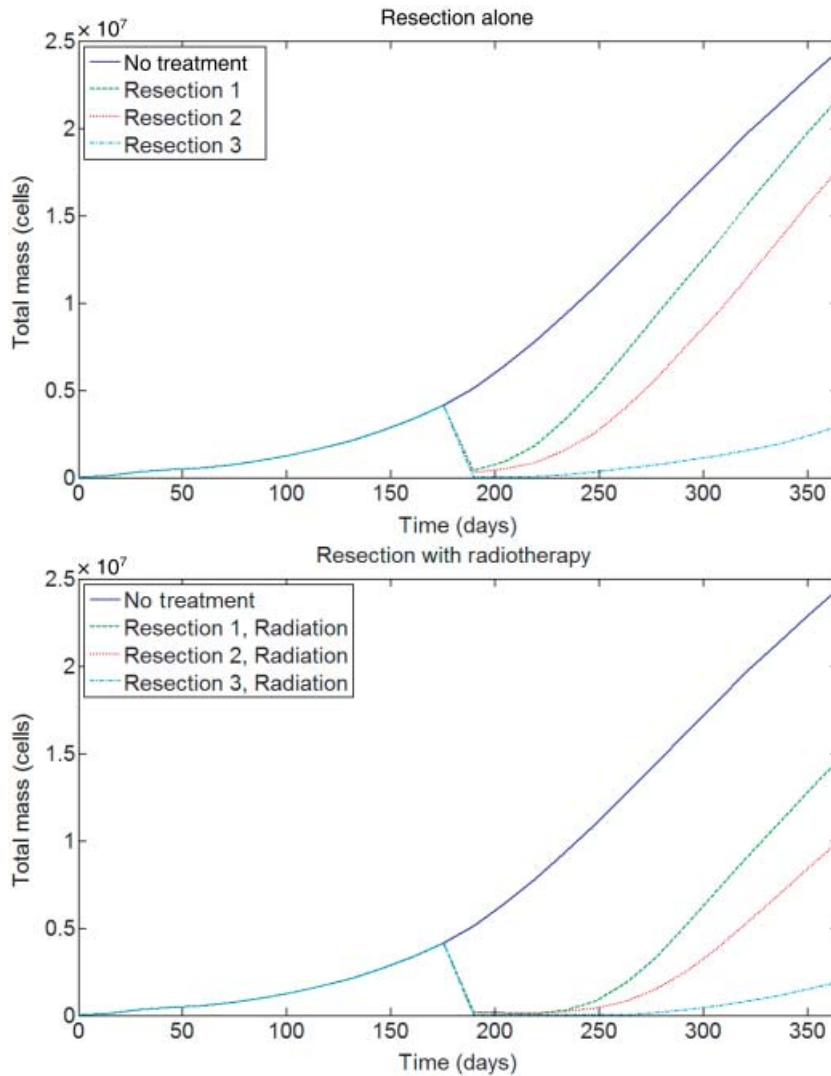


**Figure 10.** Tumour mass versus time for no treatment and for resection with the custom cavities. The resection is applied at 180 days, and the simulations are run to completion at 1 year. (a) Results without adjuvant radiotherapy, and (b) results with radiotherapy.

discrepancy between the two tumours is the failure of the simulated tumour to deform the resection cavity (a behaviour that is not allowed in this model). These results show that the model framework we have used, with the chosen parameters, can give realistic patterns of invasion on the appropriate time scale.

## Discussion

We have developed a system of stochastic partial differential equations that can predict the likely behaviour of a given GBM. It is an initial effort at a comprehensive model of the essential mechanisms that govern glioblastoma growth and invasion, and application of realistic treatments. We have attempted to synthesize previous theoretical work (7,12–14) on glioblastoma invasion into a single, unified and more realistic theoretical framework. Central to this

model is the incorporation of the ‘Go or Grow’ hypothesis, migration mediated by interaction of glioma cells with the ECM rather than simple diffusion, and the stochastic nature of the phenotypic switch.

An initial validation of the model is performed by comparing the simulation with a clinical course of invasion and treatment. The results show that this model, with parameters chosen in a reasonable range, can predict the growth of tumours over a period of many months.

By using realistic brain geometry and applying clinically realistic resection cavities to a simulated tumour, we can predict the qualitative morphology of the recurring tumour and how modifying surgical treatment affects this morphology. The stochastic nature of the model allows spatial probability distribution of tumour recurrence to be estimated, and a major goal of this work is to apply the technique to clinical cases of GBM.

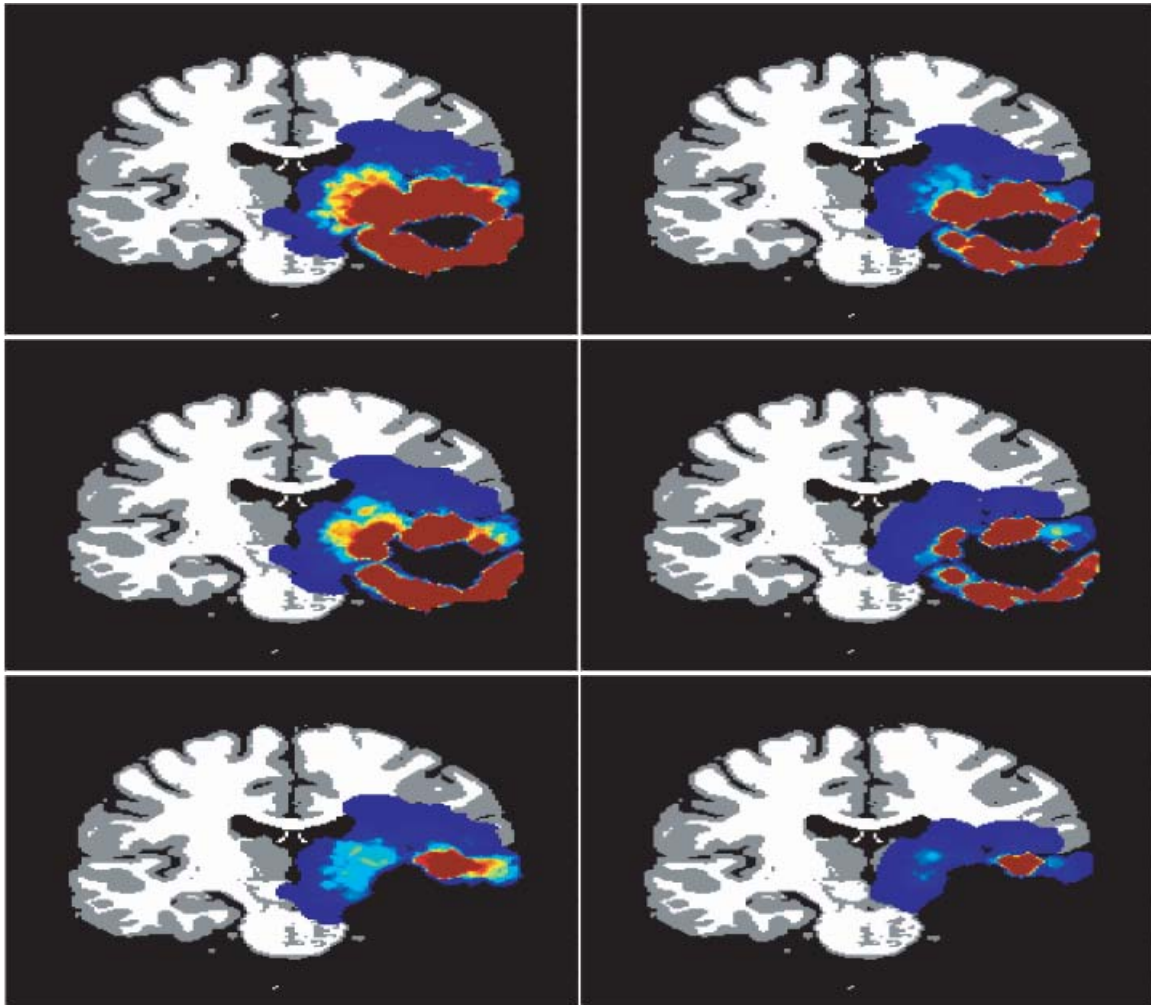


**Figure 11.** Recurring tumour for three resection cavities with and without radiotherapy. Treatment is applied at 180 days, and recurrence at 1 year is displayed. Displayed is the spatial average of 10 realizations of recurrence at a threshold for detection of 5 cells/mm<sup>2</sup>. (a) Resection 1 alone, (b) resection 1 with radiotherapy, (c) resection 2 alone, (d) resection 2 with radiotherapy, (e) resection 3 alone, and (f) resection 3 with radiotherapy.

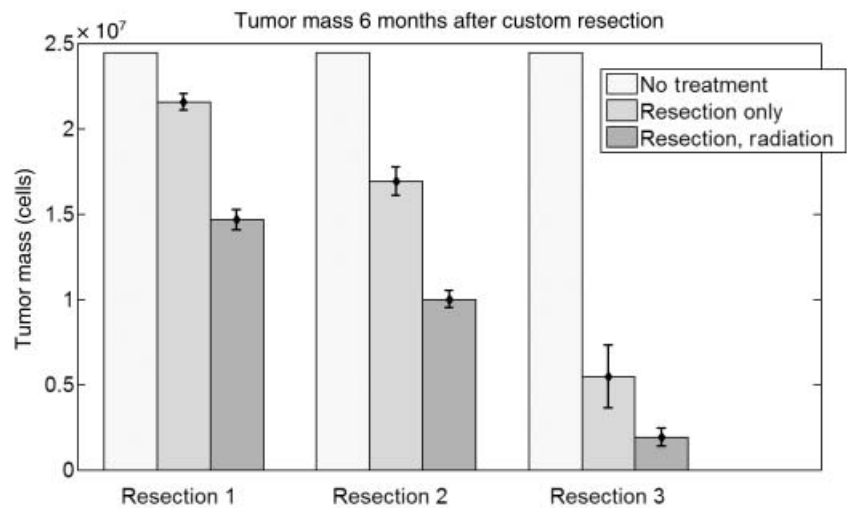


**Figure 12.** Total tumour mass 6 months following treatment for the three custom resection cavities with and without adjuvant radiotherapy. The average results for 10 recurrences are shown, and the untreated mass is included for reference for all resections.

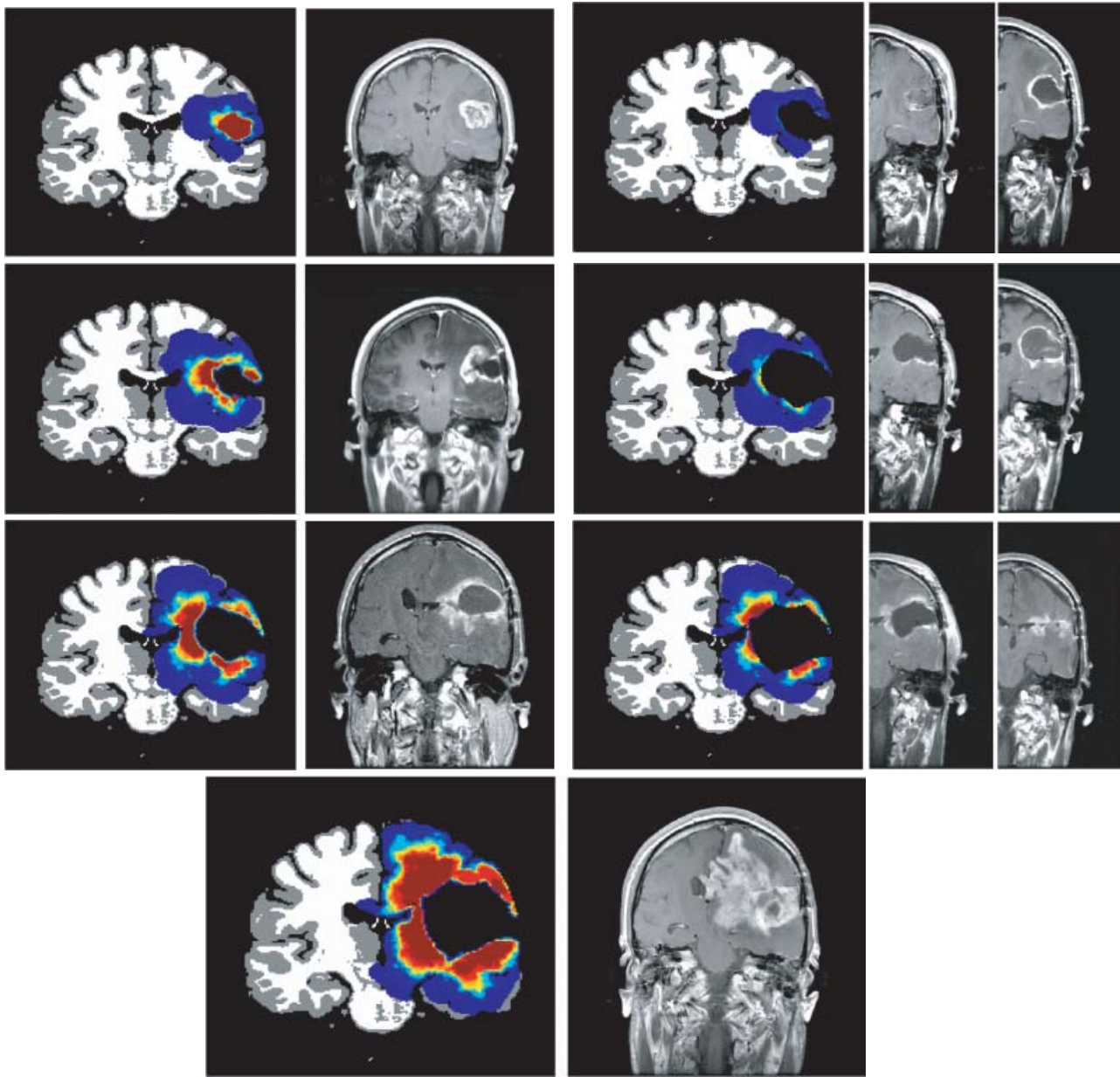


**Figure 13.** Actual and simulated course of therapy. Ten simulations are run with the results averaged in space (the same set of resection cavities is used for all simulations). The left column of panels gives the tumour at diagnosis and the two recurrent tumours. The right column displays the simulated resection cavity and the actual resection cavity at two different times following surgery. Two cavities are included to show how the cavities are deformed following surgery. The first is the cavity immediately following resection, and the second is the cavity at some later time when significant deformation has occurred. This forces a compromise to be made when choosing a simulated cavity as the form must be fit as close as possible, while at the same time an equivalent amount of tumour tissue should be removed. In addition, the cavity present when the tumour is recurring does not have the same form as it did following surgery. This highlights the inherent difficulty in using a static brain geometry. The bottom subfigure gives the final simulated and real tumours. (a) Tumour at diagnosis; (b) simulation: tumour immediately following resection at diagnosis. MRI: tumour immediately after the first resection and 82 days following the first resection. (c) First recurrence, 233 days after diagnosis; (d) simulation: tumour immediately following the second resection. MRI: tumour immediately following resection and 110 days following the second resection. (e) Second recurrence, 415 days after diagnosis; (f) simulation: tumour immediately following the third resection. MRI: tumour immediately following the third resection and 38 days following the third resection. At this point the resection cavity collapsed: a behaviour that cannot be replicated by our model. (g) Final tumour, 604 days after diagnosis.

Our simulations show that deep brain tumours invade more extensively into the surrounding brain tissue, including the ventricles, and can be expected to be more dangerous clinically.

In simulations of surgical treatment, increasing the effective resection margins significantly reduces the extent of short-term postoperative recurrence. Resections with narrow margins are little better than no treatment. With surgery alone, recurring tumours infiltrate the brain to roughly the same degree regardless of resection margins. Infiltration is reduced by combining larger resection margins with radiotherapy, indicating that aggressive resection and radiotherapy act may act synergistically.

Furthermore, our model predicts that benefit to the patient increases nonlinearly with the degree of tumour resection. This is a clear, quantitative trend that has not been suggested by clinical studies, most of which have considered less precise and more subjective measures of tumour resection, i.e. gross total resection versus partial resection, or only compared resection to biopsy (30,31). Our findings are in agreement with the more quantitative data of Lacroix *et al.* (30), who found the greatest survival benefit for tumour resection greater than 98%, and no significant survival benefit below 89%. Further quantitative retrospective clinical studies can test our predictions on resection margins.

The model yields several predictions concerning mechanisms that lead to infiltrative invasion in GBMs. Based on our sensitivity analysis, we predict that the essential contribution to malignancy of factors, such as EGF and SF/HGF, is likely not the induction of the migratory phenotype. It is more likely that these factors increase the ability of migratory cells to invade into the brain. Overall results suggest that GBM invasiveness is determined primarily by the ability of glioblastoma cells to degrade the ECM, perhaps by matrix metalloproteinase activity, the ability to migrate through a permissive ECM, and the probability that single migrating cells start a colony.

A wide variety of ECM proteins and matrix metalloproteinases increase glioma cell migration and invasiveness both *in vitro* and *in vivo* (2,21). Inhibiting these factors would likely have the effect of reducing parameters that represent ECM degradation and migration. Clinical trials of agents targeting any particular factor have been largely disappointing (2,32), suggesting that combination therapy may be necessary to significantly reduce effective parameter values. Further modelling of individual factors involved in GBM invasion may aid in rational design of such combinations.

GBMs are characterized by tortuous vasculature, regions of extreme hypoxia, necrosis, and often cystic structures. These regions are expected to form in a stochastic manner and are important in determining efficacy of treatment.

Radiation is ineffective against hypoxic cells, and irregular vasculature hampers cytotoxic drug delivery. Therefore, future models should consider the role of a stochastically evolving vasculature and its role in treatment, with the effects of radiation and chemotherapy modelled more precisely.

Our current model does not consider deformation of brain structure or oedema. These factors should be considered in future iterations of the model, as GBMs often result in significant mass effect, a major cause of morbidity (23). This is driven largely by the rapidly expanding, infiltrating nature of the tumour itself, as well as vasogenic oedema, further indicating the need to consider the role of tumour vasculature. Several authors have examined brain deformation resulting from tumour growth, using finite element approaches (33,34). We have begun work on adapting our model to a finite element framework in which invasion actively modifies brain geometry. Such a model may be used to predict how therapeutic intervention affects tumour-associated mass effect and will more accurately predict the morphology of recurring tumours.

While this model has been developed to examine *in vivo* tumour invasion, it can be easily adapted to an *in vitro* setting. Experimental work could then be performed to more accurately parameterize the model, as in the work of Stein *et al.* (13) involving glioblastoma spheroids. The ability to naturally apply *in vitro* results to a more complex *in vivo* setting is a strength of such a modelling approach.

This model has potential applications to basic science and in the clinic. It may improve our understanding of mechanisms driving infiltrative invasion; initial results suggest that cell ECM interactions and colony formation are central to malignancy. In the clinic, the model may be able to predict the likely response of a given GBM patient to various treatment regimens, thus aiding development of individual treatment plans.

## Acknowledgements

The research is partially supported by the National Science Foundation (NSF) grant DMS-0436341 and the grant DMS/NIGMS-0342388 jointly funded by the National Institutes of Health (NIH) and NSF. This project was also supported by funds from the Barrow Neurological Foundation and the Newsome Chair of Neurosurgery Research at the Barrow Neurological Institute. We would like to thank the referees for their careful reading and valuable comments and suggestions.

## References

- 1 Norden AD, Wen PY (2006) Glioma therapy in adults. *Neurologist* **12**, 279–292.

- 2 Demuth T, Berens ME (2004) Molecular mechanisms of glioma cell migration and invasion. *J. Neurooncol.* **70**, 217–228.
- 3 Tracqui P, Cruywagen GC, Woodward DE, Bartooll GT, Murray JD, Alvord EC Jr (1995) A mathematical model of glioma growth: the effect of chemotherapy on spatio-temporal growth. *Cell Prolif.* **28**, 17–31.
- 4 Woodward DE, Cook J, Tracqui P, Cruywagen GC, Murray JD, Alvord EC (1996) A mathematical model of glioma growth: the effect of extent of surgical resection. *Cell Prolif.* **29**, 269–288.
- 5 Burgess PK, Kulesa PM, Murray JD, Alvord EC (1997) The interaction of growth rates and diffusion coefficients in a three-dimensional mathematical model of gliomas. *J. Neuropathol. Exp. Neurol.* **56**, 704–713.
- 6 Tracqui P, Menjeli M (1999) Modelling three-dimensional growth of brain tumours from time series of scans. *Math. Model. Meth. Appl. Sci.* **9**, 581–598.
- 7 Swanson KR, Alvord EC, Murray JD (2000) A quantitative model for differential motility of gliomas in grey and white matter. *Cell Prolif.* **33**, 317–329.
- 8 Cocosco CA, Kollokian V, Kwan RKS, Evans AC (1997) BrainWeb: online interface to a 3D MRI simulated brain database. *Neuroimage* **5**, S425.
- 9 Kwan RKS, Evans AC, Pike GB (1996) An extensible MRI simulator for post-processing evaluation. In: Höhne KH, Kikinis R, eds. *Proceedings of the 4th International Conference on Visualization in Biomedical Computing*, Vol. 96. London, UK: Springer Verlag, pp. 135–140.
- 10 Kwan RKS, Evans AC, Pike GB (1999) MRI simulation-based evaluation of image-processing and classification methods. *IEEE Trans. Med. Imaging* **18**, 1085–1097.
- 11 Collins DL, Zijdenbos AP, Kollokian V, Sled JG, Kabani NJ, Holmes CJ *et al.* (1998) Design and construction of a realistic digital brain phantom. *IEEE Trans. Med. Imaging* **17**, 463–468.
- 12 Swanson KR, Bridge C, Murray JD, Alvord EC (2003) Virtual and real brain tumors: using mathematical modeling to quantify glioma growth and invasion. *J. Neurol. Sci.* **216**, 1–10.
- 13 Stein AM, Demuth T, Mobley D, Berens M, Sander L (2007) A mathematical model of glioblastoma tumor spheroid invasion in a 3D *in vitro* experiment. *Biophys. J.* **92**, 356–365.
- 14 MacArthur BD, Please CP, Pettet GJ (2005) A mathematical model of dynamic glioma–host interactions: receptor-mediated invasion and local proteolysis. *Math. Med. Biol.* **22**, 247–264.
- 15 Tysnes BB, Mahesparan R (2001) Biological mechanisms of glioma invasion and potential therapeutic targets. *J. Neurooncol.* **53**, 129–147.
- 16 Guillamo JS, Lisovski F, Christov C, Le Guérinel C, Defer GL, Peschanski M *et al.* (2001) Migration pathways of human glioblastoma cells xenografted into the immunosuppressed rat brain. *J. Neurooncol.* **52**, 205–215.
- 17 Werbowetski T, Bjerkvig R, Del Maestro RF (2004) Evidence for a secreted chemorepellent that directs glioma cell invasion. *J. Neurobiol.* **60**, 71–88.
- 18 Lund-Johansen M, Bjerkvig R, Humphrey PA, Bigner SH, Bigner DD, Laerum OD (1990) Effect of epidermal growth factor on glioma cell growth, migration, and invasion *in vitro*. *Cancer Res.* **50**, 6039–6044.
- 19 Brockmann MA, Ulbricht U, Grüner K, Fillbrandt R, Westphal M, Lamszus K (2003) Glioblastoma and cerebral microvascular endothelial cell migration in response to tumor-associated growth factors. *Neurosurgery* **52**, 1391–1399.
- 20 Kunkel P, Müller S, Schirmacher P, Stavrou D, Fillbrandt R, Westphal M *et al.* (2001) Expression and localization of scatter factor/hepatocyte growth factor in human astrocytomas. *Neuro-Oncology* **3**, 82–88.
- 21 Goldbrunner RH, Bernstein JJ, Tonn JC (1999) Cell-extracellular matrix interaction in glioma invasion. *Acta Neurochir.* **141**, 295–305.
- 22 Amberger VR, Hensel T, Ogata N, Schwab ME (1998) Spreading and migration of human glioma and rat C6 cells on central nervous system myelin *in vitro* is correlated with tumor malignancy and involves a metalloproteolytic activity. *Cancer Res.* **58**, 149–158.
- 23 Jain JK, di Tomaso E, Duda DG, Loeffler JS, Sorenson AG, Batchelor TT (2007) Angiogenesis in brain tumours. *Nat. Rev. Neurosci.* **8**, 610–622.
- 24 Wild-Bode C, Weller M, Rimmer A, Dichgans J, Wick W (2001) Sublethal irradiation promotes migration and invasiveness of glioma cells: implications for radiotherapy of human glioblastoma. *Cancer Res.* **61**, 2744–2750.
- 25 Thalhauser CJ, Sankar T, Preul MC, Kuang Y (2009) Explicit separation of growth and motility in a new tumor cord model. *Bull Math Biol.* **71**, 585–601.
- 26 Ohnishi T, Arita N, Hiraga S, Taki T, Izumoto S, Fukushima Y *et al.* (1997) Fibronectin-mediated cell migration promotes glioma cell invasion through chemokinetic activity. *Clin. Exp. Metastasis* **15**, 538–546.
- 27 Paemeleire K, Leybaert L (2000) Ionic changes accompanying astrocytic intercellular calcium waves triggered by mechanical cell damaging stimulation. *Brain Res.* **857**, 235–245.
- 28 Machado CML, Schenka A, Vassallo J, Tamashiro WMSC, Gonçalves EM, Genari SC *et al.* (2005) Morphological characterization of a human glioma cell line. *Cancer Cell Int.* **5**, 13.
- 29 Cotter D, Mackay D, Landau S, Kerwin R, Everall I (2001) Reduced glial cell density and neuronal size in the anterior cingulate cortex in major depressive disorder. *Arch. Gen. Psychiatry* **58**, 545–553.
- 30 Lacroix M, Abi-Said D, Fourney DR, Gokaslan ZL, Shi W, DeMonte F *et al.* (2001) A multivariate analysis of 416 patients with glioblastoma multiforme: prognosis, extent of resection, and survival. *J. Neurosurg.* **95**, 190–198.
- 31 Laws ER, Parney IF, Huang W, Anderson F, Morris AM, Asher A *et al.* (2003) Survival following surgery and prognostic factors for recently diagnosed malignant glioma: data from the Glioma Outcomes Project. *J. Neurosurg.* **99**, 467–473.
- 32 Brandsma D, van den Bent MJ (2007) Molecular targeted therapies and chemotherapy in malignant gliomas. *Curr. Opin. Oncol.* **19**, 598–605.
- 33 Wasserman R, Acharya R, Claudio S, Shin KH (1996) A patient-specific *in vivo* tumor model. *Math. Biosci.* **136**, 111–140.
- 34 Mohamed A, Davatzikos C (2005) Finite element modeling of brain tumor mass-effect from 3D medical images. In: Duncan JS, Gerig G, eds. *8th International Conference on Medical Image Computing and Computer Assisted Intervention (MICCAI 2005)*. Palm Springs, CA, USA: Springer, pp. 400–408.